Nanoscale Horizons

ROYAL SOCIETY OF CHEMISTRY

COMMUNICATION

View Article Online
View Journal

Cite this: DOI: 10.1039/d5nh00416k

Received 14th June 2025,
Accepted 29th July 2025

DOI: 10.1039/d5nh00416k

rsc.li/nanoscale-horizons

Potential-driven reaction order transitions of water oxidation on hematite photoanodes

Yanjie Liu,[a] Zhixuan Dong,[a] Qingqing Li,[a] Jundie Hu,*[a] Jiafu Qu,[a] Meiying Gong,[a] Wei Sun,[b] Chang Ming Li[ab] and Xiaogang Yang*[a]

Understanding the potential-dependent kinetics of photoelectrochemical (PEC) reactions is crucial for advancing the catalytic applications, particularly for water oxidation. This dependency arises because the accumulation of photogenerated charges, directly influenced by the applied potential, fundamentally dictates the intrinsic limitation of slow charge transfer rates. In this study, we investigated the water oxidation on hematite photoanodes with {012} facets exposed, analyzing the reaction kinetics under light and dark conditions. We found a direct correlation between the applied potential and the reaction mechanism, evidenced by a notable transition in the apparent reaction order which shifted from the 2nd- to the 4th- and then to the quasi-4th-order. This observed kinetic transition is specifically linked to the potential-driven changes in the termination and coverage of the surface oxyl intermediates.

New concepts

This work presents a new conceptual framework for understanding photoelectrochemical (PEC) oxygen evolution reaction (OER) on semiconductor photoanodes, specifically based on the behavior of pseudo-cubic hematite's {012} facets. Unlike conventional approaches that focus solely on applied potential or simplified "PV + EC" models, we demonstrate that OER kinetics on these active facets are profoundly dictated by the accumulated surface charge densities, rather than merely potential. This introduces the concept of a "rate-law of charge carriers" and represents a paradigm shift from current–voltage analyses. Our breakthrough lies in revealing an interesting potential-driven transition in the reaction order (from 2nd- to 4th-order) as a direct function of these surface intermediate coverage and charge densities, indicating dynamic shifts in multi-electron transfer mechanisms unique to these sites. This unprecedented quantitative insight differentiates our work by dissecting the intricate interplay between photogenerated charges, their accumulation, and facet-specific surface reaction pathways. It brings critical understanding to nanoscience by providing a direct link between surface charge dynamics and catalytic activity, enabling the rational design of highly efficient nanoscale photo/electrocatalysts beyond empirical optimization.

Introduction

Photoelectrochemical (PEC) water oxidation, a crucial half reaction for sustainable hydrogen production *via* water splitting,[1–3] faces persistent challenges similar to traditional electrolysis,[4] notably the sluggish four-charge transfer process and/or the requirement for high overpotential.[5] While applying high photovoltage and external bias can enhance the photogenerated charge transfer and suppress recombination, these strategies may also compromise the thermodynamic favorability of the oxygen evolution reaction (OER).[6] Recent work by Chen *et al.*[7] underscored that the photogenerated charge transfer rate at a $SrTiO_3$/electrolyte interface is proportional to the surface potential change. Interestingly, Nong *et al.*[8] found that the applied bias affected current on IrO_x electrocatalysts likely through charge accumulation. Therefore, the understanding of the elusive interplay between applied

[a] *Institute of Materials Science and Devices, School of Material Science and Engineering, Suzhou University of Science and Technology, Suzhou, 215009, P. R. China. E-mail: hjd@usts.edu.cn, xiaogang.yang@gmail.com*

[b] *Key Laboratory of Laser Technology and Optoelectronic Functional Materials of Hainan Province, Key Laboratory of Functional Materials and Photoelectrochemistry of Haikou, College of Chemistry and Chemical Engineering, Hainan Normal University, Haikou 571158, P. R. China*

Jundie Hu

Since 2020, I, Jundie Hu, have served on the Nanoscale Horizons Community Board. Over the past five years, I have actively supported the journal through initiatives including nominating emerging investigators (>20 individuals), promoting it at academic conferences, etc. Our Photocatalytic Nanomaterials Research Group is deeply honored to contribute to this landmark 10th-anniversary special issue of Nanoscale Horizons. We congratulate the journal on its first decade of excellent work and look forward to its continued outstanding contributions to nanoscience in the coming decade.

potential, surface charge and its transfer dynamics would be significant for enhancing PEC water oxidation efficiencies.

The potential sensitivity of OER electrochemical kinetics has been extensively investigated. Notably, Shinagawa *et al.* calculated that potential-dependent intermediate coverage and rate-determining step (RDS) led to a range of Tafel slopes (*e.g.*, 30, 40, 60 and 120 mV dec^{-1}) for OER electrocatalysts, extending beyond simple extreme coverage scenarios.[9] Similarly, Antipin's simulation of Tafel slopes and reaction orders (1–3), bridged surface coverage, accumulated charges and RDS.[10] Practically, it is insufficient to identify the RDS with a single Tafel slope, challenging the assumption of constant charge reactions in electrolysis.[11] In PEC systems, Durrant *et al.* reported a transition in the reaction order (*e.g.*, 1st to 3rd) of photogenerated charges with increasing charge densities, through different reaction routes.[12,13] Prof. Patzke's work further identified surface intermediates with high oxidative energy as potential active sites on hematite using rate-law analysis.[14] This complex internal voltage differences on semiconductors or electrocatalysts can vary with applied potentials even at the same surface charge densities.[15] Consequently, further investigation into charge transfer mechanisms on the photoelectrode under varied potentials is crucial for uncovering the surface intermediate coverage, RDS and ultimately improving water oxidation efficiency.[16]

Moreover, hematite (Fe_2O_3) is a strategic model photoanode for studying potential effects on the reaction order due to its controllable facets,[17,18] suitable bandgap (1.9–2.2 eV), exceptional stability,[19] and bias-assisted photo-water oxidation.[20] Density functional theory (DFT) calculations predicted energy barriers on various hematite facets, including (001),[21] (100), (210),[22] (104), (110) and (012).[23] A low Tafel slope of 58.5 mV dec^{-1} on (012) surface suggested a two-electron transfer during the RDS based on typical transfer coefficient.[23] In PEC systems, hematite exhibited a wide range of charge reaction orders (zero-, 1st-,[12,14,24] 2nd-,[24] 3rd-,[12,14,25] and 4th-orders[26]) sensitive to the charge density, pH, and test conditions. Notably, recent work by Li's group demonstrated a potential-dependent transition in charge reaction orders (0th to 4th, and back to 3rd) as the potential ranged from 0.6 V to 1.6 V *vs.* RHE,[27] indicating the reaction mechanism or RDS was indeed potential dependent. Moreover, the potential-driven modulation of surface oxy groups on hematite is supported by ATR-FT-IR studies.[24,28,29] However, uncovering the surface intermediate effect on the photoelectrochemical activities with unique crystal facets is highly essential.

Herein, we synthesized cubic hematite nanocrystals with a predominant (012) facet exposure and fabricated well-defined photoanodes. By modulating the applied potentials, we examined the potential-dependent water oxidation kinetics, linking them with surface charge densities and identifying the RDS and key intermediates. Contact angle (CA) and X-ray photoelectron spectroscopy (XPS) revealed evidence of transitions in surface intermediates induced by anodic treatments. Light-modulated transient photocurrent spectroscopy (LMTPC) and photoelectrochemical impedance spectroscopy (PEIS) were employed to elucidate how OER intermediates and surface charge were modulated by applied potential.

Results and discussion

Hematite films with the (012) facet orientation could be well assembled as a unique photoelectrode (Fig. 1a). Transmission electron microscopy (TEM) revealed uniformly shaped pseudo-cubic hematite nanocrystals with an average size of ~20 nm (Fig. 1b). High-resolution TEM (HRTEM) imaging of a tilted particle along the [$\bar{2}$21] zone axis (Fig. 1c) displayed characteristic lattice fringes, exhibiting edge angles of 86° and 94°. In Fig. 1d, fast Fourier transform (FFT) analysis of the HRTEM image yielded a quasi-square diffraction pattern, where the (01$\bar{2}$) and (102) diffractions were indexed with an inter-planar angle of approximately 86°, consistent with the [$\bar{2}$21] zone axis. The lattice spacing of 3.69 Å observed in Fig. 1e corresponded to the (012) and (102) crystallographic planes. Based on the rhombohedral symmetry ($R\bar{3}c$) of α-Fe_2O_3, the identified facets belong to the {012} plane groups or symmetrically equivalent facets. Notably, the particle size could be increased by reducing the water content in the synthesis solution. Moreover, XPS survey traces in Fig. S2 display similar curves for the hematite films treated with 0.7 V, 0.9 V and 1.3 V *vs.* RHE, confirming the existence of Fe 2p, O 1s and C 1s signals. Atomic force microscopy (AFM) image (Fig. 1f) demonstrated the successful assembly of a hematite film with the pseudo-cubic nanocrystals exhibiting preferential (012) facet exposure. The film displayed a height variation within ±15 nm, indicating a relatively ordered arrangement of the nanocubes. XRD in Fig. S3 revealed the possible (012) and (104) orientations of the annealed hematite (JCPDS, no. 33-0664) films.

A photo/electrocatalytic oxygen evolution reaction is commonly understood to proceed on a single electrochemically active site through a series of absorbed hydroxyl/oxyl intermediates, such as *, *OH, *O and *OOH (* denotes the site on the electrocatalyst). DFT calculations, as developed by Prof. Nørskov and colleagues, offer a powerful tool to depict the energy barrier landscape of the OER by considering the total energy, zero-point energy and entropy of each reaction

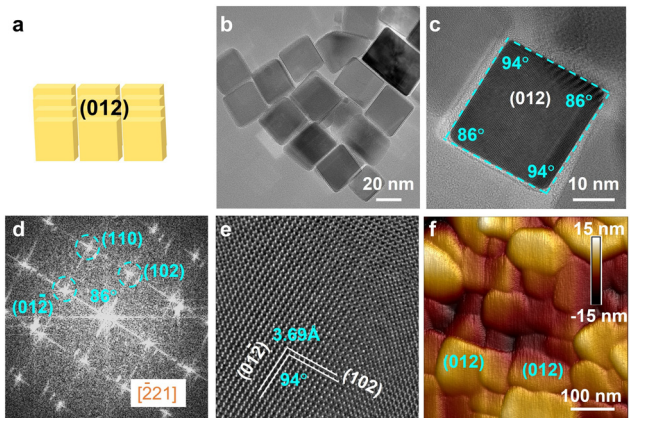

Fig. 1 Hematite nanoparticles for photoanode film preparation: (a) cartoon scheme of assembled nanocubes, (b) TEM image of hematite nanocubes, (c) HR-TEM image of hematite with (012) facet, (d) FFT pattern of hematite with the [$\bar{2}$21] zone axis, (e) HR-TEM lattice image of hematite, (f) AFM height image of the photoanode film from assembled hematite nanocubes.

intermediate (or transition state). Recognizing any of the intermediate formation steps can serve as the RDS one, we consider the *O as an initial form, analogous to the other intermediates. Importantly, a constant total energy gain of 4.92 eV is fixed for an O_2 molecular evolution within a catalytic loop.

Due to the synthetic accessibility and documented high OER activity of the hematite (012) facet, we strategically selected the (012) facet for the mechanistic study. Fig. 2a illustrates the calculated free energy barriers for a proposed serial OER routes on the hematite (012) facet under applied potentials of 0 V and 1.23 V *vs.* NHE, with data re-plotted from previous DFT calculations by Wu *et al.*[23] For consistency, the *O intermediate is selected as the initial step (energy reference), as all intermediates can be considered equivalent under steady-state catalytic conditions. Here, the most kinetically challenging step is identified as the formations of adsorbed *O from *OH (ΔG_{*O}–ΔG_{*OH} = 1.8 eV) on the hematite (012) facet, corresponding to a theoretical overpotential of 0.57 V of the RDS. At an applied potential of 1.23 V *vs.* RHE, the formation of * intermediate is thermodynamically favorable, showing a downward energy change. In contrast, the formation of *OH, *OOH and *O are thermodynamically uphill (bottom in Fig. 2a), leading to a potential-dependent shift in the rate, equilibrium constants or the intermediate coverage under steady conditions.

The four elemental reactions are detailed in Table 1, where their respective activation energies are presented. Utilizing the Erying equation ($k = (k_bT)e^{(-\Delta G/RT)}$) for the transient state of each elemental OER step,[30] the microkinetics of the four reaction steps were calculated under various applied potentials and oxygen pressure. This approach allowed us to determine the quasi-equilibrated intermediate coverages. For example, at an applied potential of 1.8 V, the calculated forward reaction constants significantly exceed the backward reaction constants, consistent with *O formation as the RDS. Under the constraint that the total coverage of all intermediate sum as unity ($\Sigma\theta = 1$), the microkinetics calculation predicts that *O and *OH dominate the surface with a coverage of 0.995 and 0.0048, respectively. It is noted that the microkinetic estimations of reaction order and rates were performed using DFT-derived energy barriers and an assumed energy barrier of 0.3 eV for transition states. While the exact potential thresholds for intermediate transitions should not be over-interpreted, this approach effectively elucidates potential-dependent trends. Further fundamental research is needed to refine these predictions.

Moreover, the strong dependence of intermediate coverage on both potential and oxygen partial pressure is illustrated with the simulated data presented in Fig. 2b, obtained by varying the potential from 0 to 2.0 V and the O_2 pressure ranging from 10^{-50} to 10^{50} bar. Since the local pressure of O_2 near the anode surface varies with the bubble size during the OER, a 1 atm partial pressure was selected for simulation which simplified the analysis. Therefore, Fig. 2c demonstrates that at 1 atm oxygen pressure ($\ln(P) = 0$), the (012) surface is predominantly covered by *, *OOH and *O under low, intermediate and high potentials, respectively. Based on our previous microkinetics study,[31] an *n*th order reaction can be observed when the *n*th charge transfer step is RDS, which involves a corresponding transfer of '*n*' charges. This dynamic governs the steady-state transitions of the OER intermediates. The 3D plot effectively visualizes these complex interactions, and offers clearer insight compared to a 2D representation. As depicted in Fig. 2d, the shift in predominant surface intermediates establishes different pre-equilibriums with corresponding charge numbers (*e.g.*, $2h^+$, $3h^+$ and $4h^+$ for * ↔ *OH ↔ *O, *OOH ↔ * ↔ *OH ↔ *O and *O ↔ *OOH ↔ * ↔ *OH ↔ *O). Therefore, the microkinetic model predicts the trend of 2nd-, 3rd- and 4th-order charge transfer reactions under increasing potentials, respectively.

The electrochemical treatments on the hematite photoanodes were carried out using a three-electrode configuration as shown in Fig. S1. For this process, specific potentials within the range of 0.7–1.4 V *vs.* RHE were applied for 40 min under dark conditions. Interestingly, this anodic activation of the hematite photoanode consistently showed increased photocurrent density–potential (*J*–*V*) curves over four consecutive linear sweeping voltammetry cycles measured in the same 1 M NaOH electrolyte. For instance, the photocurrent steadily increases from 1.17 mA cm^{-2} to 1.46 mA cm^{-2} at 1.23 V *vs.* RHE in Fig. S4a. Furthermore, the IPCE curves, measured under white LED light at 1.23 V *vs.* RHE, revealed three distinct peaks at 320, 372 nm and 398 nm in Fig. S4b. The IPCE values at 372 nm significantly improved from 27.6% to 41.0%, demonstrating a conspicuous enhancement. Additionally, Fig. S5 depicts the stability of the anodic treated iron oxide in 1 M NaOH alkaline electrolyte, with a photocurrent retention of 97% over a 3 hours test at 1.23 V *vs.* RHE. Importantly, Fig. S6a and b displayed identical UV-vis absorption spectra of hematite with/without anodic treatment. No alternation of the semiconducting nature was observed. Therefore, we are confident that the observed improvement of hematite's photoelectrochemical performance is indeed potential-sensitive anodic activation.

To unravel the potential dependence of charge transfer kinetics, we investigated the effect of anodic potentials on

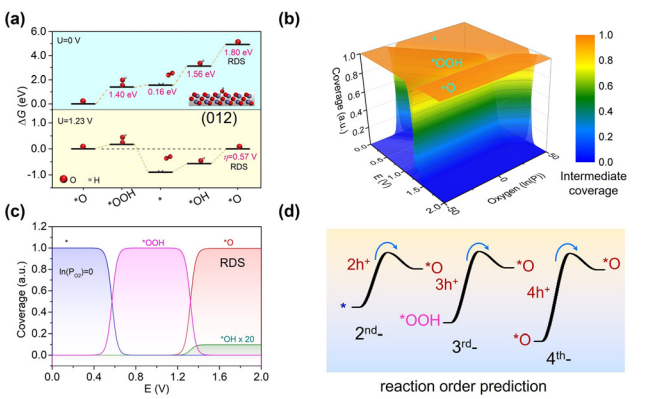

Fig. 2 OER energy diagrams of the hematite (012) facet: (a) DFT energy barriers calculated by Wu *et al.*,[23] (b) 3D map showing intermediate (*, *OOH and *O) coverage *vs.* applied potential and O_2 partial pressure, (c) intermediate coverage as a function of applied potential under ambient condition, (d) schematic uphill accumulation of charges to overcome RDS (*e.g.*, *O).

Table 1 Reaction rate constants, activation energy and intermediate coverage of hematite {012} facets

Reaction	k_f	k_b	K (k_f/k_b)	ΔG (eV)	E_{af} (eV)	Site	Coverage
$* + HO^- + h^+ \leftrightarrow *OH$	8.86×10^{11}	5.27×10^{7}	1.68×10^{4}	−0.24	0.06	*OH	0.0048
$* + HO^- + h^+ \leftrightarrow *O + H_2O$	5.27×10^{7}	5.27×10^{7}	1	0	0.30	*O	0.995
$* + HO^- + h^+ \leftrightarrow *OOH$	3.04×10^{14}	5.27×10^{7}	5.77×10^{6}	−0.4	−0.10	*OOH	9.6×10^{-6}
$*OOH + HO^- + h^+ \leftrightarrow * + O_2 + H_2O$	2.78×10^{35}	5.27×10^{7}	5.27×10^{27}	−1.64	−1.34	*	1.4×10^{-4}

Note: under a potential of 1.8 V, 1 atm O_2 pressure, pH = 14 and water concentration of 55.5 M assuming that the transient state for activation energy of the forward reaction ($E_{a,f}$) is 0.3 eV larger than those calculated through DFT calculations (ΔG_n).

charge accumulation and transfer behaviors within hematite photoanodes. Fig. 3a presents transient current curves under UV illumination (30 mW cm^{-2}), demonstrating a continuous increase in photocurrent density (to 1.13 mA cm^{-2}) with the potential increased from 0.9 V to 1.5 V *vs.* RHE. Concomitantly, clear negative spikes were observed upon switching light off. Further details on PEC performance under period chopped UV light are provided in Fig. S6. While cyclic voltammetry (CV) profiles under dark conditions in Fig. S7a showed only a gentle increase of capacitive charges, the CV sweeps in Fig. S7b unequivocally demonstrated an enhancement in PEC reactivity after the anodic treatment at increasing potentials. Given that the steady dark current is negligible (~ 0) and the overpotential for the OER on hematite is >0.3 V,[32] it is reasonable to assume that the surface charge diminishing (due to leakage) was minimal below 1.5 V under dark conditions. Thus, the surface charges (stored in negative spikes, inset in Fig. 3a) are mainly scavenged by the backflow of current from FTO side rather than by bulk recombination in space charge layer. By integrating these negative spikes over time, charge densities at each applied potential were quantified (pink column in Fig. 3b). The red curves indicate surface charge density increases from 0.51 nm^{-2} to 1.94 nm^{-2} with a maximum at 1.0 V *vs.* RHE. On the other hand, at each potential, the surface charges (Q) are calculated according to the capacitor equation ($Q = C \cdot V_{ph}$), where C and V_{ph} were obtained from the simulation of PEIS and photovoltage measurements at the trapping sites (or surface states). The brown columns in Fig. 3b show the surface charge densities of 3.35, 3.88, 1.79, and 2.02 per nm^2 at potentials of 0.70, 0.90, 1.2, and 1.4 V *vs.* RHE, respectively. We observed that the charge densities obtained by integrating of TPC profile (pink columns) showed a similar potential dependence to those measured by PEIS, albeit with consistently lower values. Roughly, both PEIS and TPC techniques demonstrate maximum charge accumulation on hematite within the 0.9–1.0 V potential range, a behavior consistent with surface

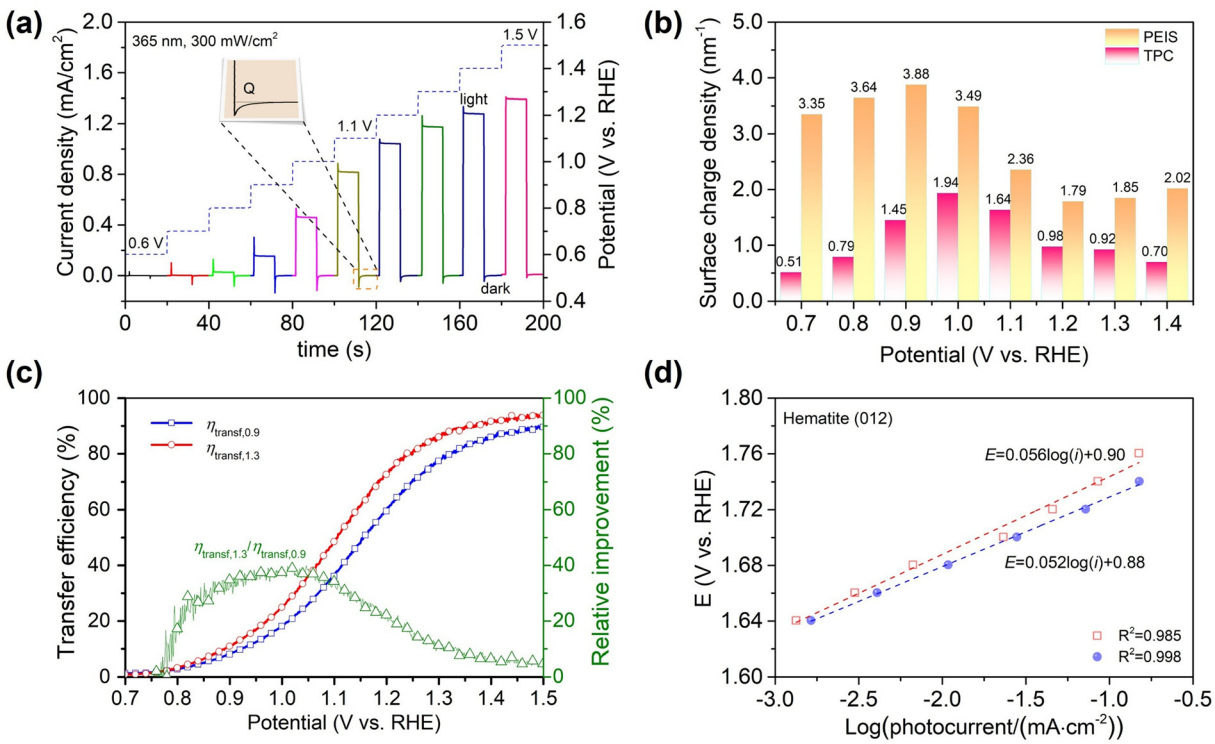

Fig. 3 The potential-sensitive PEC performance of hematite: (a) transient photocurrent spectra with chopped UV light illumination (365 nm, 30 mW cm^{-2}), (b) accumulated surface charge density through PEIS and TPC, (c) charge transfer efficiencies increment by anodic treatment at 0.9 V and 1.3 V *vs.* RHE, (d) Tafel slopes of hematite at 0.9 V and 1.3 V *vs.* RHE under dark conditions.

capacitance under variable potentials.[33,34] Their discrepancy can be attributed to the minimal contribution from surface capacitive charge in the TPC method, coupled with the possible overestimation of surface states in the PEIS method. Despite this charge density being higher than some recently reported values,[35] the general potential dependence exhibited a similar trend.

To analyze the efficiency of the OER, we assumed a charge transfer efficiency of unity for photooxidation of H_2O_2. The resulting OER charge transfer efficiencies were plotted in Fig. 3c, revealing a trend which was calculated based on $J_{OER}/J_{H_2O_2}$ from J–V curves (Fig. S8). Compared with the sample anodically treated at 0.9 V, transfer efficiencies significantly increased from 8.2% at 0.9 V to 77.3% at 1.3 V. Similarly, for the sample treated at 1.3 V, efficiencies rose from 11.0% to 85.9% over the same potential range. It is clear that the relative increment (open triangles) of transfer efficiency exceeds 35% within 0.9–1.0 V window, indicating the anodic treatment's most pronounced effect region occurs near the onset potential. In Fig. 3d, the Tafel slope of the hematite films under dark conditions are measured at 52 mV dec^{-1} and 56 mV dec^{-1}, treated under a potential of 0.9 V (blue curve) and 1.3 V (red curve) *vs.* RHE, respectively. According to the Tafel equation (TS = 2.303$RT/(\alpha nF)$),[36] and assuming a charge transfer coefficient (α) of 0.5, these values corresponded an n = 2 electron transfer in the rate-determining process. Following this, we investigated the power-law relationship between accumulated charges and potential, aiming to discover the underlying causes of lower charge transfer efficiencies observed at lower applied biases.

To further evaluate the charge reaction kinetics, the PEIS were measured on hematite, where the equivalent circuit was shown in Fig. 4a. As suggested before, the trapped surface states ($R_{ct,trap}$ and $C_{ct,trap}$) can host photogenerated charge, as the catalytic process. The capacitance of these active sites, measured by PEIS, showed that the trend is potential sensitive in Fig. 4b: mostly, the larger one exists near the onset potential, ranged from 7.23 μF cm^{-2}, to 12 μF cm^{-2} and 5.58 μF cm^{-2} from 0.7 to 1.4 V, suggesting a charge accumulation balanced between generation and transfer/recombination. The photovoltage of the hematite is also sensitive to the light illumination densities, which showed a logarithm trend in Fig. 4c. By multiplying the capacitance and voltage dropped on trap states, the accumulated surface charges were obtained at each potential. In Fig. 4d, an interesting logarithmic dependence of charge density on the potential is expressed by the trend (*e.g.*, $\log(Q) \propto V$) under different potentials. For example, the 0.9 V-treated hematite exhibited the highest charge accumulation (red squares), which strongly corroborates the charge density results $\left(Q = 0.177 \cdot \ln\left(\frac{I}{11.35}\right)\right)$ like the photovoltaics. To discover the power order of charge reaction kinetics, we analyzed the steady photocurrent densities and surface charge densities. It is noted that the photocurrent represents charge transfer rates, when we assume the surface charge recombination is negligible across the wide potential window.[12] Briefly, the relationship between the charge transfer rate (J_{photo}) and charge density Q is expressed by a power law:[37]

$$-\frac{dQ}{dt} \approx J_{photo} = k_n Q^n \quad (1)$$

where k_n is the rate constant and n is the reaction order, respectively. The reaction order n can be extrapolated from the

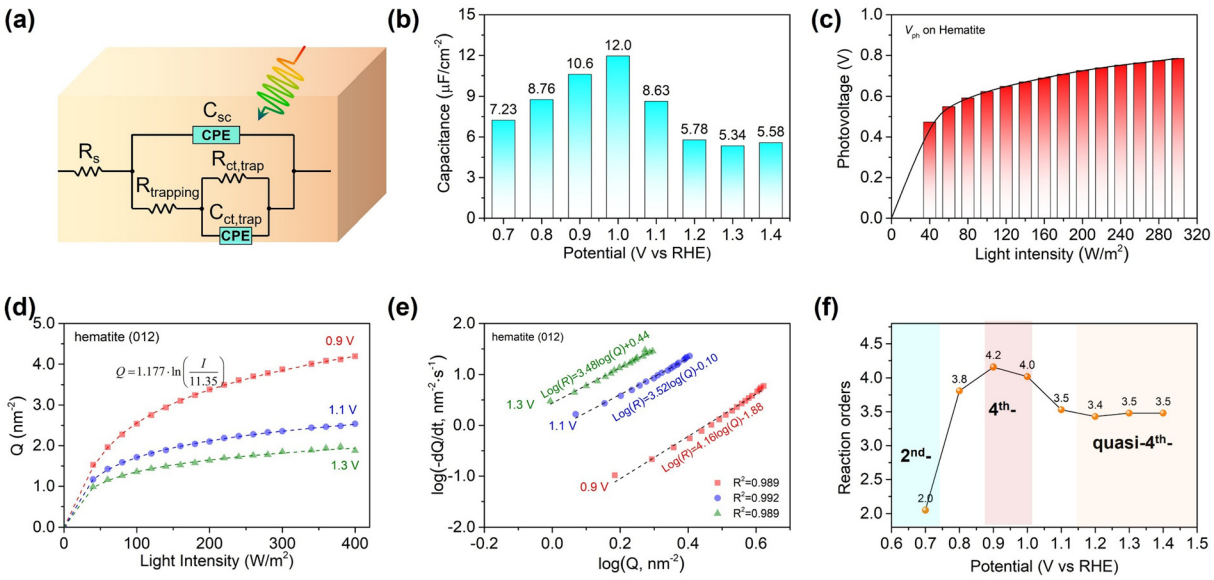

Fig. 4 Charge reaction order of the OER on anodically treated hematite photoanodes: (a) schematic representation of the hematite photoanode with its electrochemical equivalent circuit by PEIS, where $R_{ct,trap}$ and $C_{ct,trap}$ denote the resistance and capacitance of the trapped surface charge sites, respectively, (b) $C_{ct,trap}$ of the surface state measured at various potentials, (c) photovoltage of hematite generated under various light illuminations, (d) trend of surface charge density as a function of light intensity for hematite treated with different potentials, (e) charge reaction order for hematite treated with different potentials, and (f) charge reaction kinetics/orders of hematite at various potentials.

logarithm–logarithm (log–log) plots:

$$\log\left(-\frac{dQ}{dt}\right) = \log k_n + n\log Q \quad (2)$$

Using the surface charge density and steady water oxidation photocurrent measurements treated at various potentials (*e.g.*, Fig. S9a and c), the rate-law of charge reaction kinetics was derived. In Fig. 4e, the linear trend of $\log(-dQ/dt)$ *versus* $\log(Q)$ of the hematite photoanodes activated at 0.9 V, 1.1 V, and 1.3 V (*vs.* RHE) showed slopes of 4.16, 3.52, and 3.48, respectively. These values (4 ± 0.5) suggest that the water oxidation reactions are likely to follow a 4th-order (or a combination of 4th-order and 3rd-order) dependence of the charge density, coincided with recent observations by Li *et al.*[27] It was shown that the rate constants for hematite increased from $10^{0.07}$ to $10^{1.54}$, under increased potentials and at unit charge densities (*e.g.*, 1 nm^2). In Fig. 4f, the reaction order from PEIS charge density analysis increased from an initial value of 2.0 when anodic treated at 0.7 V, then to 3.8 at 0.8 V, showing a maximum reaction order of 4.16 at 0.9 V. A similar reaction order trend derived from different LMTPC results further elucidates the kinetics, showing a 0.2 V higher potential required for anodic treatment to achieve 4th order reactions. In Fig. S10c, the reaction order was closer to 3.0–3.2 at potential ~0.9 V. This rate-law analysis reveals that surface charge reaction rates and reaction orders are strongly correlated with applied potentials and the possible alternation of various intermediates (*e.g.*, *, *OOH, or *O combinations). Furthermore, using a double-layer capacitance model, the electrochemical surface area (ECSA) of hematite was found to decrease from 0.64 cm^2 to 0.40 cm^2 as the potential increased in Fig. S11, using a reference value of 28 μF cm^{-2} for hematite. This phenomenon eliminated the possibility of surface area enhancement to the reactivity, suggesting that the observed kinetic behavior should be more due to the catalytic activity. Combined with the microkinetics calculations in Fig. 2 and previous calculations, the possible reaction orders could range from 2nd-, 3rd-, and 4th-order in a potential range wider than those in Fig. 4. Notwithstanding, this high coincidence of the experimental results and predictions have shown that the charge reaction order for the OER can be modulated by the potentials' variation. It is noted that at potentials higher than 1.1 V, the obtained quasi-fourth orders (*e.g.*, 3.5th) were possibly due to the combination of lower reaction portion, or relative lower charge densities, or some charge recombination, which require more profound studies. Here, we will focus on verify the possible surface intermediate alternation indeed sensitive to the anodic treatment at various potentials.

Because the planar (012) hematite facets do not possess high surface area, applying ATR-FT-IR detection through operando analysis faces great challenges. We aimed to use contact angle and XPS techniques as *ex situ* methods to characterize intermediate changes. Fig. 5a–d display that the contact angles on the hematite surface increase from 57.9° to 83.2°, 110.5°, and 125.9° when subjected to anodic treatment potentials ranging

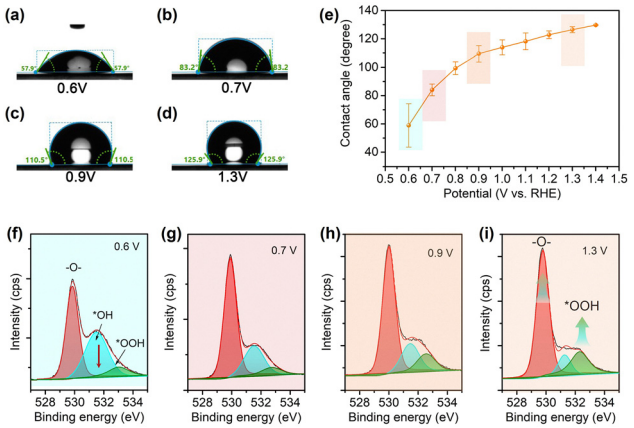

Fig. 5 (a)–(d) Water contact angle plots on hematite treated under various applied potentials. (e) Water contact angle trend in the potential window (0.6 V to 1.4 V). (f)–(i) O 1s XPS binding energy spectra of hematite films.

from 0.6 V to 1.3 V *vs.* RHE, respectively. The consistently increasing contact angle indicated a decrease in surface hydrophilicity and an increase in hydrophobicity. This change is likely to alternate the polarity or hydrogen bonding of surface functional terminations. Fig. 5e summarizes that the water contact angles on hematite generally increase as the applied potentials shifted positively from 0.6 V to 1.4 V *vs.* RHE, thereby confirming the trend of decreasing hydrophilicity under higher anodic potentials. This increase in the contact angle signifies the transition of Fe_2O_3 towards a more hydrophobic state after prolonged anodic treatment, or due to the conversion from *OH to *, *O, and *OOH intermediates. This phenomenon is similar to the contact angle measurement of Fe_3O_4 particles,[38] which increase from −1.0 V to 0.2 V (*vs.* Ag wire).

Next, XPS spectra of the O 1s band (Fig. 5f and i) demonstrate a transition of surface oxyl (hydroxyl) intermediates. In Fig. 5f, the O 1s peak could be divided into three components, with binding energies at 529.4 eV, 531.05 eV, and 532.58 eV, corresponding to lattice oxygen, surface hydroxyl (*OH) termination, and oxyl (*O) and hydroperoxide (*OOH) termination, respectively.[39] For example, the *OH termination decreased significantly from 40.7% to 24.9%, 19.2%, and 9.9%, as shown in Table S1. Conversely, the *OOH (or *O) termination increased from 5.5% to 11.9% and 20.2% at 0.7 V, 0.9 V, and 1.3 V, respectively. This intermediate conversion has been discovered by ATR-FT-IR[24] and operando FT-IR[28] analysis. Additionally, Fig. S12 is the binding energy spectra of Fe 2p for hematite, where Fe $2p_{1/2}$ is located at 724.2 eV for untreated films. The Fe $2p_{3/2}$ peak is attributed to two components at 711.2 eV and 709.7 eV for Fe^{3+} and Fe^{2+}, respectively. Anodic treatment of hematite at 1.3 V induced a negative shift (0.2 eV) of these binding energies. With the anodic potential increase, the conversion of oxidation state and intermediate decrease the hydrophilicity of the hematite surface.

This work investigated the impact of potential on surface intermediates and their termination in photoelectrochemical oxygen evolution reactions on hematite (012) facets, a factor

often overlooked by the simplified "PV + EC" model.[40] While thermodynamically reasonable regarding charge flow, this concept often failed to accurately describe kinetic behaviors, as charge transfer on a photoelectrode surface fundamentally differs from that on common electrocatalysts.[41] Unlike dye-sensitized solar cells, PEC water oxidation systems typically involve higher-order, multiple-charge transfer reactions, rather than simple first-order kinetics.[42] This study specifically reveals a complex landscape of multiple-charge transfer reactions on hematite, demonstrating a remarkable transition in the reaction order from 2nd- to 4th- (potentially *via* 3rd-) under the influence of varying potentials.

Next, we utilized DFT calculations to map energy barrier heights, which not only revealed the RDS but also allowed us to predict the trend of charge accumulation with varying potential. Through this thermodynamically favorable process, we simulated the trend of intermediate coverage domination on the surface, assuming the RDS limits the overall reaction kinetics. Under the pre-equilibrium assumption before the RDS and a steady-state assumption after the RDS, the reaction order can sometimes equal the number of charges required to overcome the RDS.[31] Thus, through this simple anodic treatment across different potentials, we demonstrated the potential for surface intermediate-controlled photocharge transfer kinetics in PEC systems.

However, several pitfalls are inherent in these mechanistic interpretations: first, the precise detection of surface intermediates remains challenging, particularly for the most active, transient species that serve as catalytic sites, whereas more dominant (potentially inert) species may not exhibit significant changes. Second, DFT calculations primarily provide thermodynamically stable snapshots of intermediates rather than capturing the transient states relevant to transition state theory (*e.g.*, the Eyring equation), suggesting that the pre-equilibrium assumption may not always be strictly accurate. Third, the assumption of surface charge densities derived from a capacitor model requires a deep understanding of PEC systems and photovoltage measurements, areas that are still under active investigation.

Conclusions

We investigated the intricate relationship between applied potential, surface charge accumulation, and charge transfer kinetics during photoelectrochemical oxygen evolution reactions on hematite. Using PEIS and LMTPC techniques, we observed that surface charge accumulation peaked between 0.9 and 1.0 V *vs.* RHE before decreasing at higher potentials. This trend was corroborated by contact angle changes, which suggested a shift from hydrophilic hydroxyl-terminated species to more hydrophobic intermediates. Crucially, our analysis ruled out significant contributions from band structure or Fermi level shifts. By examining the relationship between hole transfer rate and surface hole density, we discovered an interesting potential-dependent shift in reaction order: it rose from the 2nd-order to the 3rd, then to 4th-order near peak surface charge densities, stabilizing at 3.5rd-order around 1.3–1.4 V. This work fundamentally underscores the profound impact of intermediate species on OER mechanisms in PEC systems, offering new insights for material design in energy applications.

Experimental sections

All the chemical reagents are commercially obtained from Sinopharm Chemical Reagent (Shanghai) and Titan-Tansoole Lab shop (Shanghai Titan Technology Co. Ltd.), used without further purification. The FTO substrate (F-SnO_2, 7 Ω per square, South China Xiangcheng Technology Co.) was ultrasonically cleaned prior to use.

Synthesis of hematite nanocubes (HNCs)

HNCs exposing the (012) facet were synthesized based on the reaction of Fe(acetylacetonate)$_3$ and NaOH in oleic acid, ethanol and water (v/v = 1/1/1), according to the previous methods.[43] In a Teflon-lined stainless-steel autoclave, the mixture of 0.353 g (or 1 mmol) Fe(acetylacetonate)$_3$ and 3 mmol NaOH in an oleic acid (5 mL), ethanol (5 mL) and water (5 mL) solution, was heated in an oven at 200 °C for 24 h. The products were classified *via* centrifugation at 500 rpm for 3 min three times and dispersed in ethanol before use.

Synthesis of planar hematite films

The hematite films were hydrothermally deposited on a clean FTO substrate in 0.5 mM ferric ammonium oxalate at 150 °C for 12 hours, and annealed at 800 °C for 4–6 min, according to a previous report.[44] The hematite (012) nanocubes were loaded on the planar hematite film by drop casting of ethanol dispersion using PEI as an assembling stabilizer, after which the films were quickly annealed at 800 °C for 5–6 min. Due to the internal built-in electric field requirement (avoiding a too fast response) and diffusion effect (*e.g.*, 2–4 nm) for hematite,[45] a relative thick layer (80–100 nm) of the films were applied, where the surface holes either stored at the surface active sites or in space charge layer (SCL) nearby displayed longer lifetime, facilitate the further rate-law study.

Materials characterization

The size, morphology, crystalline facets, surface components and photoelectric properties of hematite films are investigated using various instruments that are shown in the SI. Briefly, the hematite nanoparticles and films were characterized on transmission electron microscopy (HR-TEM), X-ray diffractometry (XRD, Cu Kα), UV-vis absorption, atomic force microscopy (AFM, ScanAsyst tip), X-ray photoelectron spectroscopy (XPS, Al Kα), and contact angle analyzer, respectively.

Photoelectrochemical measurements

Typically, the hematite on FTO was cut into a 5 mm × 5 mm size, fabricated into devices with Cu wire connected to the FTO layer with Ag paste, and all other test areas were insulated with crosslinked silicon rubber. All the PEC measurements were

carried out using a three-electrode configuration (hematite as the working electrode, Pt wire as the counter electrode, and Hg/HgO (1 M NaOH, 0.098 V *vs.* NHE) as the reference electrode) on an electrochemical workstation (CH Instrument, 760E). To evaluate the potential effect, a constant anodic potential ranging from 0.7 V to 1.4 V (*versus* RHE) for 30–60 minutes was applied on hematite photoanodes in NaOH under dark conditions (shown in Fig. S1). The polarization current–potential (*J*–*V*) curves were recorded under simulated sunlight illumination (Perfectlight, AM 1.5G, 100 mW cm^{-2}). The incident photon-to-current efficiency (IPCE) curves were measured with a CIMPS-QE/IPCE, using the tunable light resource (TLS 03 and UV-light).

The photogenerated charge densities at the hematite surface were investigated using simple capacitor model as Zhang *et al.* presented.[24] Briefly, the surface charge densities were also evaluated through the simplified capacitor assumption ($Q = C{\cdot}V_{ph}$), where the capacitance (C) and voltage drop (V_{ph}) were derived from an equivalent circuit (R(C(R(RC)))) for photoelectrochemical impedance spectroscopy (PEIS) and onset potential gain from the *J*–*V* polarization curves ($V_{ph} = V_{dark} - V_{light}$, 0.03 mA cm^{-2} as the threshold) under the same varied LED illuminations. Moreover, the surface charges were also calculated using cathodic transient integration, where a light-modulated transient photocurrent (LMTPC)[46] measurement was carried out on a workstation (Zahner, CIMPS), using UV LED light (λ = 365 nm, intensities varying from 40 to 400 W m^{-2}). Remarkably, the background dark current was maintained close to zero. The charge densities and photocurrent densities were applied for extrapolate the rate-law of the OER.

Author contributions

Y. L., Z. D. and Q. Li performed materials and PEC experiments, J. Q. performed XPS analysis, M. G. synthesized films, W. S. and C. M. L. validation and provide resources, Y. L. wrote original draft. J. H. and X. Y. performed conceptualization, data verification and supervised the project. All authors reviewed and edited the manuscript.

Conflicts of interest

There are no conflicts to declare.

Data availability

The data supporting this article have been included as part of the SI. Original experimental data and outputs of microkinetics calculations are available *via* Science Data Bank, **https://www.scidb.cn/en/s/rq2uQv**.

Includes experimental details, XRD, XPS, UV-vis absorption, CV, *J*–*V*, IPCE, and other measurements. See DOI: **https://doi.org/10.1039/d5nh00416k**

Acknowledgements

We gratefully acknowledge the financial support provided by the Natural Science Research Project in Jiangsu Province (Project BK20231342), the National Natural Science Foundation of China (Project 22008163), and the Natural Science Foundation of Jiangsu Province (Project BK20210867). This work also received support from the Hainan Province Flexible Talent Introduction Collaborative Innovation Center.

Notes and references

1 R. Chen, L. Meng, W. Xu and L. Li, *Small*, 2024, **20**, 2304807.
2 X. Yang and D. Wang, *ACS Appl. Energy Mater.*, 2018, **1**, 6657–6693.
3 A. Vilanova, P. Dias, T. Lopes and A. Mendes, *Chem. Soc. Rev.*, 2024, **53**, 2388–2434.
4 A. Govind Rajan, J. M. P. Martirez and E. A. Carter, *ACS Catal.*, 2020, **10**, 11177–11234.
5 T. E. Jones, D. Teschner and S. Piccinin, *Chem. Rev.*, 2024, **124**, 9136–9223.
6 W. Yang, R. R. Prabhakar, J. Tan, S. D. Tilley and J. Moon, *Chem. Soc. Rev.*, 2019, **48**, 4979–5015.
7 R. Chen, D. Zhang, Z. Wang, D. Li, L. Zhang, X. Wang, F. Fan and C. Li, *J. Am. Chem. Soc.*, 2023, **145**, 4667–4674.
8 H. N. Nong, L. J. Falling, A. Bergmann, M. Klingenhof, H. P. Tran, C. Spöri, R. Mom, J. Timoshenko, G. Zichittella, A. Knop-Gericke, S. Piccinin, J. Pérez-Ramírez, B. R. Cuenya, R. Schlögl, P. Strasser, D. Teschner and T. E. Jones, *Nature*, 2020, **587**, 408–413.
9 T. Shinagawa, A. T. Garcia-Esparza and K. Takanabe, *Sci. Rep.*, 2015, **5**, 13801.
10 D. Antipin and M. Risch, *Electrochem. Sci. Adv.*, 2023, **3**, e2100213.
11 Y.-H. Fang, G.-F. Wei and Z.-P. Liu, *J. Phys. Chem. C*, 2014, **118**, 3629–3635.
12 F. Le Formal, E. Pastor, S. D. Tilley, C. A. Mesa, S. R. Pendlebury, M. Grätzel and J. R. Durrant, *J. Am. Chem. Soc.*, 2015, **137**, 6629–6637.
13 C. A. Mesa, L. Francàs, K. R. Yang, P. Garrido-Barros, E. Pastor, Y. Ma, A. Kafizas, T. E. Rosser, M. T. Mayer, E. Reisner, M. Grätzel, V. S. Batista and J. R. Durrant, *Nat. Chem.*, 2020, **12**, 82–89.
14 J. Li, W. Wan, C. A. Triana, H. Chen, Y. Zhao, C. K. Mavrokefalos and G. R. Patzke, *Nat. Commun.*, 2021, **12**, 255.
15 G. Righi, J. Plescher, F.-P. Schmidt, R. K. Campen, S. Fabris, A. Knop-Gericke, R. Schlögl, T. E. Jones, D. Teschner and S. Piccinin, *Nat. Catal.*, 2022, **5**, 888–899.
16 Y.-M. Kim, Y. Hong, K. Hur, M.-S. Kim and Y.-M. Sung, *ACS Appl. Mater. Interfaces*, 2023, **15**, 37290–37299.
17 J. Ouyang, J. Pei, Q. Kuang, Z. Xie and L. Zheng, *ACS Appl. Mater. Interfaces*, 2014, **6**, 12505–12514.
18 W. Li, K. R. Yang, X. Yao, Y. He, Q. Dong, G. W. Brudvig, V. S. Batista and D. Wang, *ACS Appl. Mater. Interfaces*, 2019, **11**, 5616–5622.

19 B. K. Jha, S. Chaule and J.-H. Jang, *Mater. Chem. Front.*, 2024, **8**, 2197–2226.
20 J. Li, H. Chen, C. A. Triana and G. R. Patzke, *Angew. Chem., Int. Ed.*, 2021, **60**, 18380–18396.
21 P. Liao, J. A. Keith and E. A. Carter, *J. Am. Chem. Soc.*, 2012, **134**, 13296–13309.
22 X. Zhang, C. Cao and A. Bieberle-Hütter, *J. Phys. Chem. C*, 2016, **120**, 28694–28700.
23 H. Wu, T. Yang, Y. Du, L. Shen and G. W. Ho, *Adv. Mater.*, 2018, **30**, 1804341.
24 Y. Zhang, H. Zhang, A. Liu, C. Chen, W. Song and J. Zhao, *J. Am. Chem. Soc.*, 2018, **140**, 3264–3269.
25 J. Zhang, Q. Lin, Z. Wang, H. Liu, X. Li and Y. Zhang, *Small Methods*, 2021, **5**, 2100976.
26 X. Yang, Z. Zheng, J. Hu, J. Qu, D. Ma, J. Li, C. Guo and C. M. Li, *iScience*, 2021, **24**, 103500.
27 D. Li, R. Wei, H. Yin, H. Zhang, X. Wang and C. Li, *Chem. Sci.*, 2023, **14**, 1861–1870.
28 O. Zandi and T. W. Hamann, *Nat. Chem.*, 2016, **8**, 778–783.
29 S. Liu, L. Wu, D. Tang, J. Xue, K. Dang, H. He, S. Bai, H. Ji, C. Chen, Y. Zhang and J. Zhao, *J. Am. Chem. Soc.*, 2023, **145**, 23849–23858.
30 R. Chang, *Physical Chemistry for the Biosciences*, University Science Books, 2005.
31 G. Cao, J. Hu, J. Qu, J. Jin and X. Yang, *Catal. Lett.*, 2023, **153**, 138–149.
32 H. C. Nguyën, F. A. Garcés-Pineda, M. de Fez-Febré, J. R. Galán-Mascarós and N. López, *Chem. Sci.*, 2020, **11**, 2464–2471.
33 L. Palmolahti, H. Ali-Löytty, R. Khan, J. Saari, N. V. Tkachenko and M. Valden, *J. Phys. Chem. C*, 2020, **124**, 13094–13101.
34 B. Klahr, S. Gimenez, F. Fabregat-Santiago, T. Hamann and J. Bisquert, *J. Am. Chem. Soc.*, 2012, **134**, 4294–4302.
35 T. Liu, W. Li, D. Z. Wang, T. Luo, M. Fei, D. Shin, M. M. Waegele and D. Wang, *Angew. Chem., Int. Ed.*, 2023, **62**, e202307909.
36 S. Anantharaj and S. Noda, *Mater. Today Energy*, 2022, **29**, 101123.
37 G. Cao, J. Hu, Y. Wang, J. Qu, D. Ma, J. Jin, W. Sun, X. Yang and C. M. Li, *Appl. Surf. Sci.*, 2023, **613**, 156081.
38 R. Zhang, M. Song, X. Li, Z. Guan and X. Wang, *Anal. Bioanal. Chem.*, 2006, **386**, 2075–2079.
39 J.-C. Dupin, D. Gonbeau, P. Vinatier and A. Levasseur, *Phys. Chem. Chem. Phys.*, 2000, **2**, 1319–1324.
40 P. Chatterjee, M. S. K. Ambati, A. K. Chakraborty, S. Chakrabortty, S. Biring, S. Ramakrishna, T. K. S. Wong, A. Kumar, R. Lawaniya and G. K. Dalapati, *Energy Convers. Manage.*, 2022, **261**, 115648.
41 X. Yang, C. Du, R. Liu, J. Xie and D. Wang, *J. Catal.*, 2013, **304**, 86–91.
42 L. M. Peter, K. H. Bevan and E. Ponomarev, *Electrochim. Acta*, 2024, **493**, 144422.
43 O. Elishav, D. Stone, A. Tsyganok, S. Jayanthi, D. S. Ellis, T. Yeshurun, I. I. Maor, A. Levi, V. Beilin, G. E. Shter, R. Yerushalmi, A. Rothschild, U. Banin and G. S. Grader, *ACS Appl. Mater. Interfaces*, 2022, **14**, 41851–41860.
44 K. Wang, X. Yang, P. Li, Y. Zhao, X. Wang and Z. Zheng, *ChemNanoMat*, 2016, **2**, 681–687.
45 X. Zong and C. Li, in *Metal Oxides in Heterogeneous Catalysis* ed. J. C. Védrine, Elsevier, 2018, pp. 355–399, DOI: **10.1016/B978-0-12-811631-9.00007-7**.
46 J. Jin, J. Hu, J. Qu, G. Cao, Y. Lei, Z. Zheng, X. Yang and C. M. Li, *ACS Appl. Mater. Interfaces*, 2022, **14**, 17509–17519.